Journal of
Ceramic Science
and Technology

*J. Ceram. Sci. Technol.*, **11** [1] 36-43 (2020)
DOI: 10.4416/JCST2019-00063
available online at: http://www.ceramic-science.com


# $(K_{0.5}Na_{0.5})NbO_3$-$Ba(Zn_{1/3}Nb_{2/3})O_3$ Lead-Free Ceramics: Transmittance and Microstructure

**Chenwei Li[1], Xin Xu[1], Zhenlin Lu[*1]**

[1]School of Materials Science and Engineering, Xi'an University of Technology, Xi'an 710048, People's Republic of China.

received August 21, 2019; received in revised form November 28, 2019; accepted December 18, 2019

**Abstract**

**Lead-free transmittance electro-optic ceramics $(1-x)(K_{0.5}Na_{0.5})NbO_3$-$xBa(Zn_{1/3}Nb_{2/3})O_3$ (x = 0.03, 0.05, 0.07, 0.08, 0.09 and 0.11) (KNN-BZN) were prepared with the solid-state reaction technique. The effects of $Ba(Zn_{1/3}Nb_{2/3})O_3$ dopant content on the microstructure, phase transition, optical property, and electrical properties were studied systematically. The X-ray-diffraction and Raman spectroscopy results indicated that for KNN-BZN ceramics with increasing BZN content, the crystal structure transforms from the orthorhombic phase into the pseudo-cubic phase and finally to the tetragonal phase. The KNN-BZN ceramics (0.05 mm thickness) with x = 0.07 exhibited the highest transmittance of 43.00 % in the visible spectrum, which was due to the high relative density, low porosity, uniform microstructures, and high symmetry of the pseudo-cubic structure. Moreover, $\varepsilon_r$, tanδ, $P_r$ and $E_c$ are 975.9, 0.02, 2.231 μC/cm$^2$ and 9.82 kV/cm, respectively. All of the above demonstrated that the KNN-$x$BZN ceramics could be promising lead-free transparent piezoceramics.**

*Keywords: Transparent ceramics, linear transmittance, phase structure*

## I. Introduction

Compared with metal materials, traditional ceramic materials have good thermal stability, corrosion resistance and wear resistance [1]. However, in some special fields, such as optical computers, electronic information technology, and national defense and military applications, traditional ceramics are often not viable. Therefore, researchers have turned their attention to transparent ceramic materials. Transparent ceramics can be divided into transparent ferroelectric ceramics, transparent scintillating ceramics, transparent infrared ceramics, and transparent laser ceramics according to their different functions [2]. Among transparent ferroelectric ceramics, only a few can be used commercially at present. Haertling and Land first prepared La-doped lead zirconate titanate ceramics $[(Pb_{1-x}La_x)(Zr_yTi_{1-y})_{1-x/4}O_3$ (PLZT)] by means of hot-pressing sintering. PLZTs are good relaxation ferroelectrics that exhibit large quadratic photoelectric coupling coefficients, so they are widely used in the manufacturing of anti-strong-radiation goggles [3,4]. PLZTs can also be used as rarefied ferroelectric ceramics for optical storage, showing a linear photoelectric coupling effect. $(1-x)Pb(Mg_{1/3}Nb_{2/3})O_3$-$xPbTiO_3$($0.1 < x < 0.35$) and $(1-x)Pb(Zn_{1/3}Nb_{2/3})O_3$-$xPbTiO_3$($0.15 < x < 0.35$) have been developed and put into commercial use in recent years [5,6]. Both of these ceramics are relaxation ferroelectrics with perovskite structure, which exhibit a strong quadratic photoelectric coupling effect. However, since the content of lead oxide – a toxic and volatile substance – is up to 60 %, this leads to an irreversible impact on human health and the ecological environment in the process of production and use. Owing to the increasing awareness of environmental protection, researchers have turned their attention to lead-free piezoelectric transparent ceramics. Sodium potassium niobate (KNN) lead-free piezoceramics are one of the potential candidates that has been studied in depth [7–12].

The main factors affecting transparent ferroelectric ceramics include the raw materials, sintering process, pores, surface finish, and crystal structure. From the perspective of crystal structure, the high symmetry of ceramic materials having a cubic structure makes it easier for materials to exhibit transparency [13,14]. A previous study showed that doped ions enter the KNN lattice, and the orientation and form of lattice distortion are different due to the differences in occupying position and ion radius [15,16]. An oxygen octahedron expands by replacing B-site ions of the KNN lattice with larger ions or ion groups, and the lattice collapses towards the center of oxygen octahedron by replacing A-site ions of the KNN lattice with smaller ions or ion groups. Under the joint action of the two, the O-phase of the KNN lattice evolves toward the R phase. Moreover, it is well known that $ABO_3$ materials are ferroelectrics of perovskite type exhibiting a relaxor-type diffuse phase transition. Therefore, based on consideration of the above factors, $Ba(Zn_{1/3}Nb_{2/3})O_3$ was doped in the KNN ceramics, and $Ba^{2+}$(1.35 Å) and $Zn^{2+}$(0.74 Å) are suitable for introduction into $K^+$(1.33 Å) and $Nb^{5+}$(0.7 Å), respec-

* Corresponding author: lvzl2002@xaut.edu.cn

tively. In addition, effects of $Ba(Zn_{1/3}Nb_{2/3})O_3$ content on the phase transition, microstructure, optical properties, and electrical properties of $(1-x)(K_{0.5}Na_{0.5})NbO_3$-$xBa(Zn_{1/3}Nb_{2/3})O_3$ ceramics were investigated in detail.

## II. Experimental Procedures

$(1-x)(K_{0.5}Na_{0.5})NbO_3$-$xBa(Zn_{1/3}Nb_{2/3})O_3$ (KNN-BZN, x = 0.03, 0.05, 0.07, 0.08, 0.09 and 0.11) ceramics were prepared using an ordinary sintering method. The starting powders were $Na_2CO_3$ (99.9 %), $K_2CO_3$ (99.9 %), $Nb_2O_5$(99.95 %), $BaCO_3$ (99 %), and $ZnO_2$ (99 %). The raw materials were first dried in a vacuum oven at 80 °C for 5 h to remove absorbed moisture. The mixed KNN-BZN powders were ball-milled with ethanol using zirconia balls for 10 h and then pre-sintered at 800 °C for 3 h. After calcination, all the powders were ball-milled again with ethanol for 10 h and then pressed into disk samples with a PVA binder at 300 MPa; the diameter of the disk samples was 15 mm. The samples were then sintered at 1 180 °C for 6 – 8 h in air. Before measurement, all the obtained ceramics were thinned to a thickness of ~ 0.5 mm and polished to make both the surfaces smooth. Silver electrodes were fired at 800 °C for 10 min on the top and bottom surfaces of the sintered samples. The ceramics were poled under a DC field of 3 – 4 kV/mm at 90 °C in silicon oil for 15 min. Microstructures were examined with scanning electron microscopy (SEM, JSM-6700F). Crystalline structures were characterized by means of X-ray diffraction (XRD) analysis with Cu Kα radiation (X' Pert PRO X-ray). Raman spectra (LabRAM HR Evolution) were recorded in order to characterize the crystal structure. The optical transmittance of the samples was measured by means of ultraviolet-visible-near-infrared (UV-vis-NIR) spectroscopy (PE Lambda950). The relative permittivity $\varepsilon_r$ and loss tangent tanδ were measured as a function of temperature using an impedance analyzer (Agilent E4980A). Room-temperature polarization-electric field (P-E) loops were measured with a ferroelectric tester (aixACCT TF200) at 1 Hz.

## III. Results and Discussion

The XRD patterns of the $(1-x)$KNN-$x$BZN transparent ceramics are shown in Fig. 1. It can be concluded that the ceramic crystal structures of different compositions are perovskite structures. To further observe the change in crystal structure, the diffraction peaks between 30° – 34° and 44° – 48° were amplified. It can be found that with increasing BZN content, the diffraction peak at approximately 46° changes from the (002) and (020) double peaks that exhibit the left peak is low and the right peak is high relative to the single (200) peak, and then shift for the (200)/(002) doublet exhibiting that the left peak is high and the right peak is low. Moreover, when $x = 0.07$, the unit-cell parameters a = 3.95662, c = 3.939954, and the a/c value is close to 1, indicating that the phase transition of the KNN-BZN ceramics first changes from the orthorhombic phase to the pseudo-cubic phase, and then changes from the pseudo-cubic phase to the tetragonal phase. The diffraction peak at approximately 32° in the figure tends to shift toward a small angle with increasing BZN content, which can be considered an increase in the lattice constant owing to doping [17].

In addition to observation of the changes in ceramics structure by means of XRD, Raman spectroscopy can be used to analyze the phase composition of different materials based on their specific Raman spectra. The Raman spectra of ceramics with different BZN contents measured at room temperature are shown in Fig. 2(a). It can be seen from the figure that KNN-BZN and pure KNN ceramics have similar Raman spectra in the range 200 – 1 000 $cm^{-1}$. The vibration modes of the $NbO_6$ oxygen octahedron in the figure are expressed as $1A_{1g}(\tau_1) + 1E_g(\tau_2) + 2F_{1u}(\tau_3, \tau_4) + F_{2g}(\tau_5) + F_{2u}(\tau_6)$ ($\tau$ is the frequency band, and $A_{1g}$, $E_g$, $F_{1u}$, $F_{2g}$ and $F_{2u}$ represent different vibration modes), indicating that doped BZN enters the KNN lattice [18].

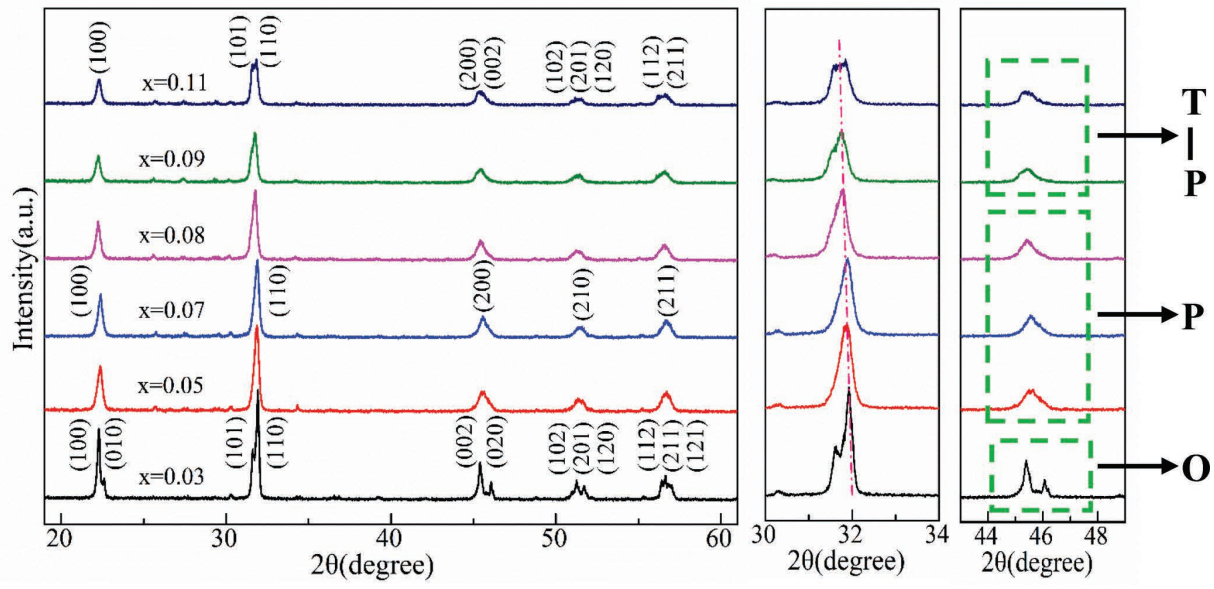


**Fig. 1:** XRD patterns of (1-$x$)KNN-$x$BZN ceramics.

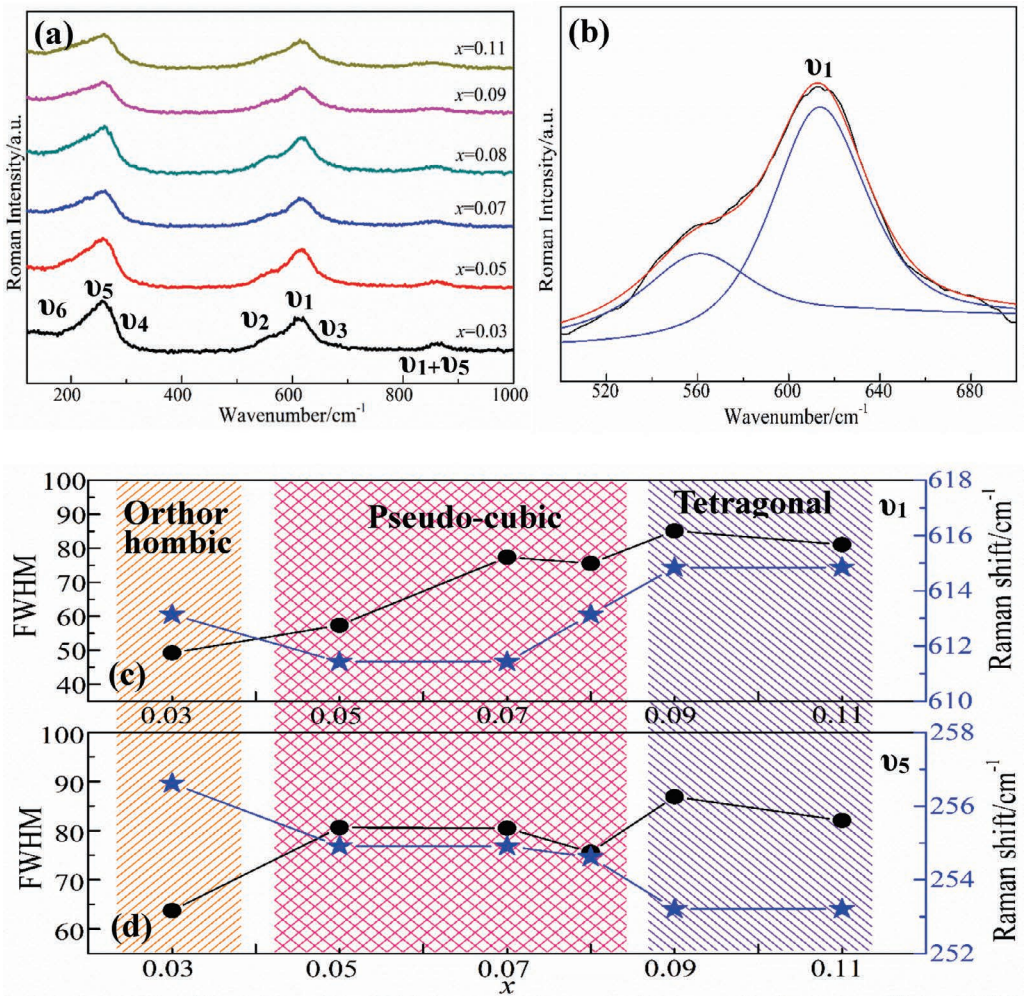


**Fig. 2:** (a) Raman spectra of (1-*x*)KNN-*x*BZN ceramics; (b) $\tau_1$ mode fitted using Gaussian-function modes. Raman shift and FWHM of (c) $\tau_1$ and (d) $\tau_5$ modes.

$\tau_1$ represents the stretching vibration of the $NbO_6$ oxygen octahedron along the c axis and $\tau_5$ represents the bending vibration along the shear direction. To study the change in the crystal structure of KNN-BZN ceramics, we performed Gaussian fitting on $\tau_1$ and $\tau_5$. Fig. 2(b) shows the results of $\tau_1$ Gaussian fitting for KNN-0.03BZN, and the corresponding frequency and full width at half-maximum (FWHM) are counted, as shown in Fig. 2(c) and (d). The results show that for (1 –*x*)KNN-*x*BZN ceramics, with increasing BZN doping, the Raman shift of the $A_{1g}(\tau_1)$ vibration mode shifts to the low frequency and then to high frequency, while the $F_{2g}(\tau_5)$ vibration mode shifts to low frequency. It is indicated that when the composition of the ceramics in the system is between $x = 0.05$ and 0.08, the lattice stretches along the c axis caused by the B-site doping and the pseudo-cubic phase appears. When $x > 0.08$, the amount of $Ba^{2+}$ substituted for the A-site ion increases, and the large electro-negative A-site ion induces a larger molecular field, resulting in the collapse of the lattice along the shear direction. At this time, the tetragonal phase appears, which is consistent with the previous XRD analysis. For the FWHM, the $\tau_1$ and $\tau_5$ mode becomes broader because of BZN doping. It can be considered that the crystallinity and doping affect the dynamic coupling of the vibration modes of the oxygen octahedron.

The natural surface morphology of the KNN-BZN ceramics with different concentrations was measured by means of SEM as shown in Fig. 3. It can be seen from the figure that when $x = 0.03$, 0.05 and 0.07, (1 –*x*)KNN-*x*BZN ceramics have clear grain boundaries and grain stacking growth. When $x \geq 0.08$, voids are formed, the compactness decreases, and the grain boundaries are blurred. In addition, the grain size of the ceramic samples are obviously component-dependent. As the doping content increases, the grain size of the ceramic sample changes significantly, and the grain size is not uniform. To observe the distribution of doped elements in ceramics, the distribution of elements in KNN-0.05BZN ceramics was characterized. As shown in Fig. 4, all doped elements are evenly distributed in the ceramics without segregation, indicating that all doped ions enter into the KNN lattice.

The effect of BZN content on the grain-size distribution and relative density was further studied. Fig. 5 shows the average grain size and relative density of KNN-BZN ceramics with the change of BZN content. It can be seen from the figure that the average grain size of ceramics first decreases rapidly and then decreases slowly, while the relative density first increases and then decreases. Generally speaking, when $x = 0.07$, the average grain size

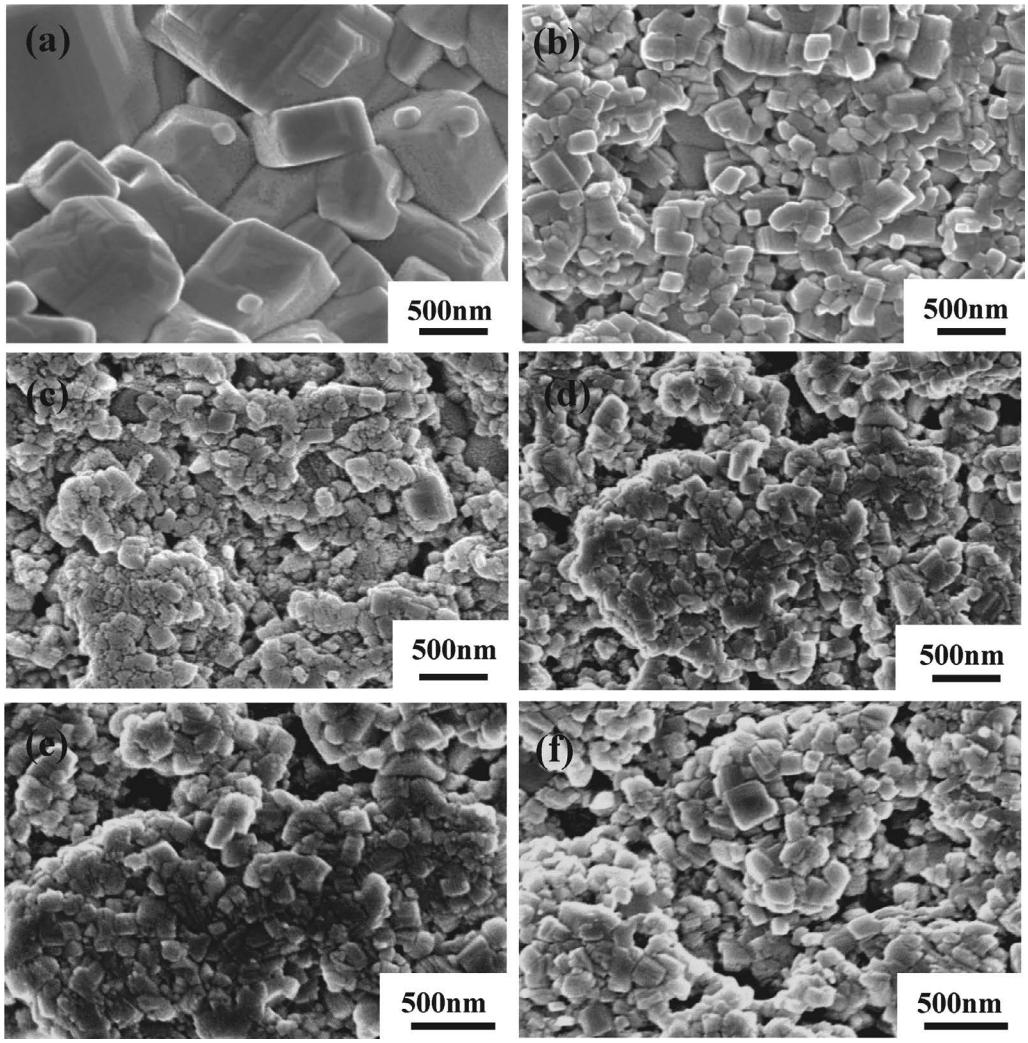


**Fig. 3:** SEM images of natural surface microstructures of (1-*x*)KNN-*x*BZN ceramics.

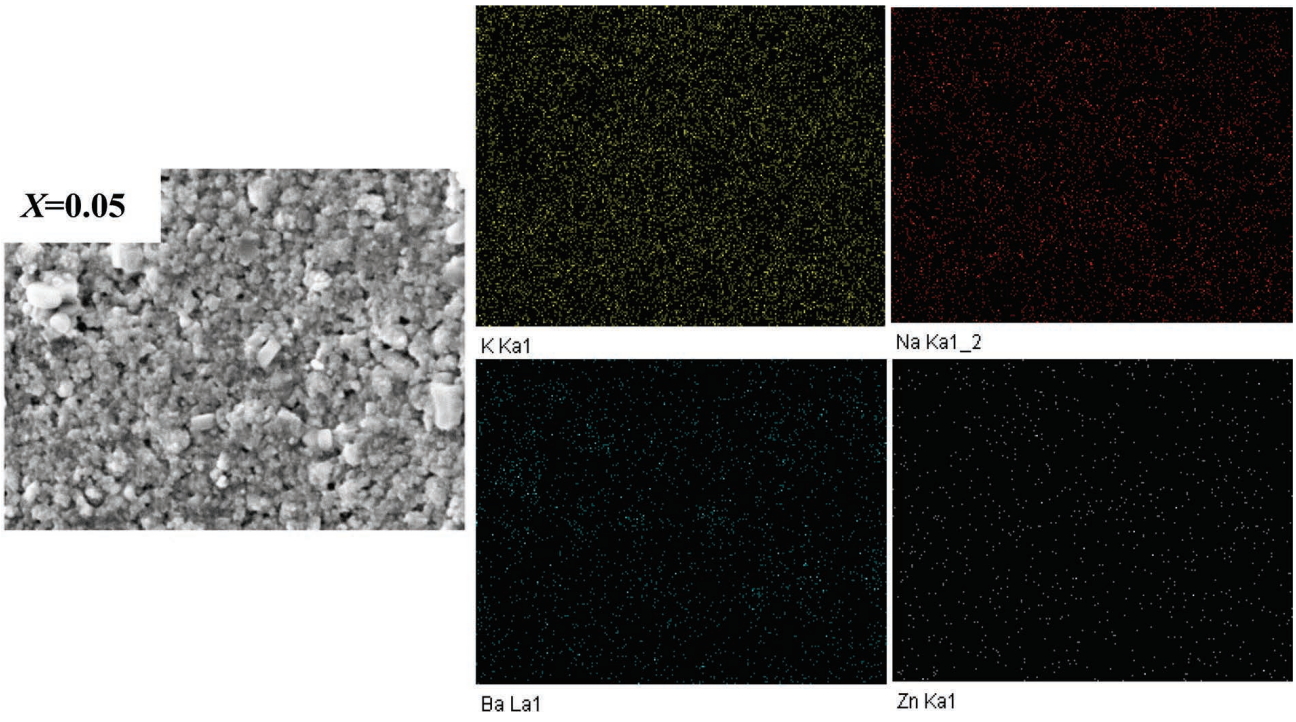


**Fig. 4:** SEM images of (1-*x*)KNN-*x*BZN ceramics with x = 0.05 and corresponding element mapping.

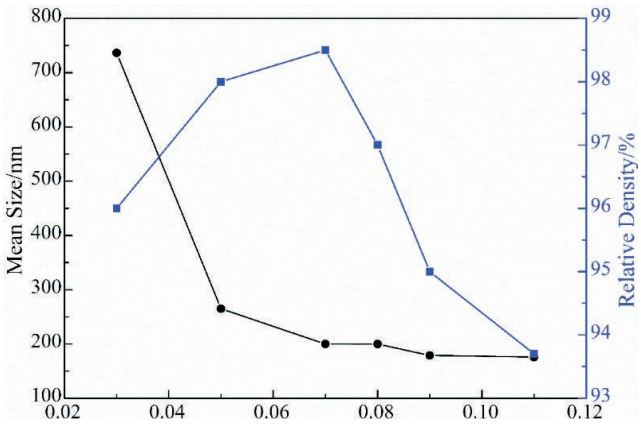


**Fig. 5:** Effect of grain size and relative density on the composition $x$ of (1-$x$)KNN-$x$BZN ceramics.

and relative density are the best, as are the optical properties of this component. One of the main reasons is that the grain size is fine, and the density is good, so the light scattering caused by pores is less. At this time, better transparency can be obtained.

The KNN-BZN samples were polished to a thickness of 0.5 mm, and then the samples were visually observed and photographed, as shown in Fig. 6(a), which shows that with increasing BZN content, the handwriting becomes clear and then blurred again. When $x = 0.07$, the handwriting is clear, indicating that the 0.93KNN-0.07BZN ceramic sample has the best transmittance. This is consistent with the results obtained from the crystal structure, grain size and relative density of the samples. Fig. 6(b) shows the linear transmittances of all components at 1 272 nm and 780 nm, representing the transmittances of each component in the near-infrared and visible regions, respectively. It can be seen that with increasing doping amount, the linear transmittance of ceramics in both the visible and near-infrared regions first increases and then decreases, and reaches the maximum at a doping amount of 0.07. However, it can be seen the maximum transmittance in the visible region is only 43 % (780 nm). Obviously, the doping of BZN does not make the transparency of KNN-based ceramics achieve our desired effect. Combined with the analysis of microstructure, this may be due to the uneven grain size and unclear grain boundary of KNN-BZN composition series, which are not ideal and have an effect on linear transmittance. However, compared with the linear transmittance of pure KNN in the visible region of 20 – 30 %, the introduction of BZN improves the transmittance of ceramics to a certain extent [19].

Fig. 7 shows the dielectric temperature spectrum of (1 –$x$)KNN-$x$BZN ceramic samples. As observed, when $x = 0.03$ and 0.11, the peak of phase transformation from the orthogonal phase to tetragonal phase occurs at 160 °C and 180 °C, respectively. When $x = 0.07$, the peak of phase transformation from the pseudo-cubic phase to cubic phase can only be observed in the dielectric temperature spectrum, which indicates that the phase structure of (1 –$x$)KNN-$x$BZN ceramics also changes with increasing BZN content from the orthogonal phase to pseudo-cubic phase, and eventually becomes the tetragonal phase, which is consistent with the results obtained by means of XRD and Raman spectroscopy. In addition, with increasing BZN doping, the phase transition peak of the ceramics has broadened — that is the diffusion phase transition (DPT) — which is a kind of relaxation behavior that is beneficial to improving the linear transmittance [20]. Moreover, the dielectric loss of all ceramics is less than 2 % between room temperature and 400 °C, which is advantageous for improving the properties of ceramics. At the same time, it can be found from Table 1 that the Curie temperature $T_c$ and dielectric constant of the sample have the opposite trend. The Curie temperature first decreases and then increases, and the dielectric constant first increases and then decreases. In summary, the (1 –$x$)KNN-$x$BZN ceramic system designed in the present work has the best performance when $x = 0.07$, and the dielectric constant is 975.9.

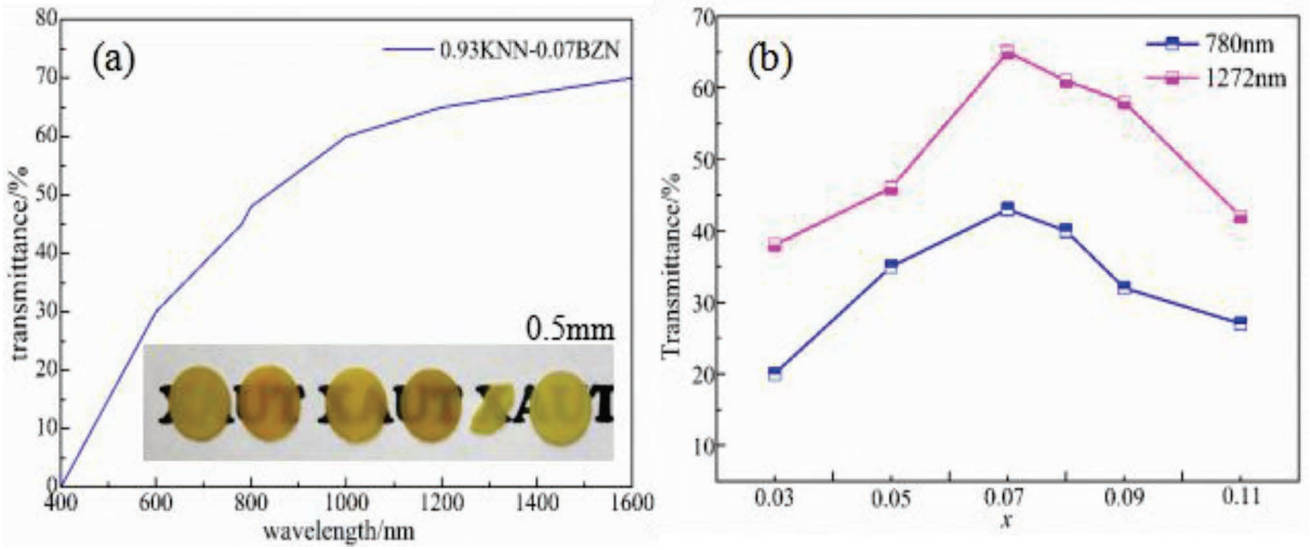


**Fig. 6:** Transmission spectra of (1-$x$)KNN-$x$BZN ceramics. (a) Transmittance of 0.93KNN-0.07BZN specimen and photographs (specimens with $x = 0.03$, 0.05, 0.07, 0.08, 0.09 and 0.11 from left to right above the letters) in the inset. (b) Optical transmittance of (1-$x$)KNN-$x$BZN for light at wavelengths of 1 272 and 780 nm.

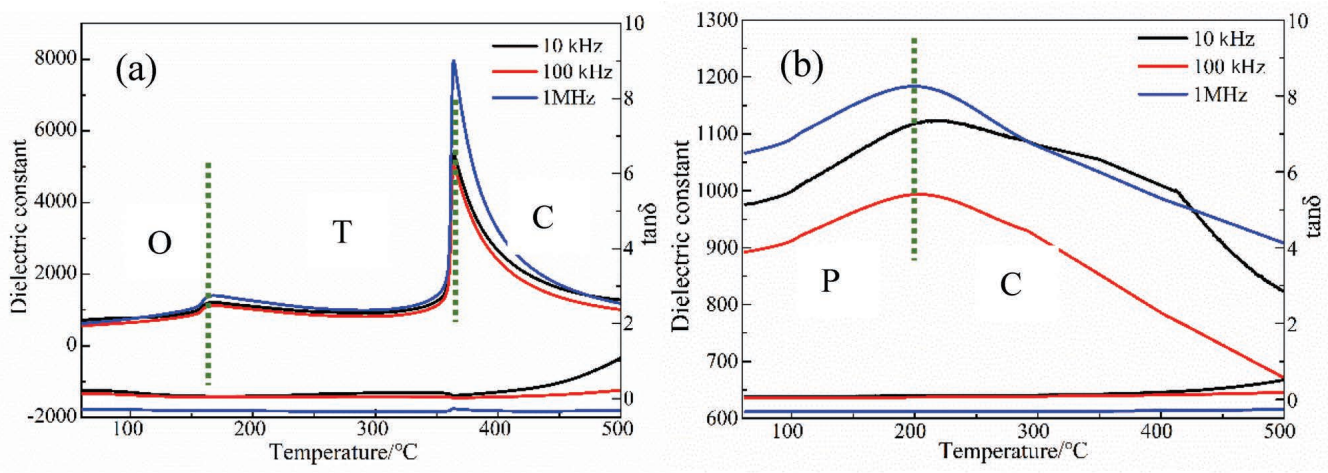


| $x$ | Tc(°C) | $\varepsilon_r$(10 kHz) |
|---|---|---|
| 0.03 | 363 | 710.3 |
| 0.05 | 300 | 720.5 |
| 0.07 | 208 | 975.9 |
| 0.08 | 206 | 970.4 |
| 0.09 | 308 | 942 |
| 0.11 | 322 | 897.5 |

Table 1 Permittivity and Curie temperature of (1-$x$)KNN-xBZN ceramics

**Fig. 7:** Temperature and frequency dependence of dielectric permittivity and corresponding loss for (1-$x$)KNN-$x$BZN ceramics, (a) $x$ = 0.03, (b) $x$ = 0.07, and (c) $x$ = 0.11.

According to Fig. 7(b), we determined that 0.93KNN-0.07BZN ceramics have relaxation characteristics. It is well known that the normal ferroelectrics should obey the Curie-Weiss law above the Curie temperature, the Curie-Weiss formula is expressed as follows [21]:

$$\varepsilon = \frac{C}{T - T_{CW}} \quad (1)$$

$$\Delta T_m = T_B - T_M \quad (2)$$

$$\frac{1}{\varepsilon} - \frac{1}{\varepsilon_m} = \frac{(T - T_m)^y}{C} \quad (3)$$

where $C$ is the Curie-Weiss constant, $T_{CW}$ the Curie-Weiss temperature, $T_B$ the Burns temperature (the starting point for observing the Curie-Weiss law), and $T_m$ the temperature at which the maximum value of $\varepsilon_m$ is obtained. At the same time, the diffusion factor $\gamma$ is the main parameter used to distinguish between normal ferroelectrics and ideally relaxing ferroelectrics. When $\gamma = 1$, the material is a normal ferroelectric; when $1 < \gamma < 2$, it is a relaxation ferroelectric; and when $\gamma = 2$, it is an ideal relaxation ferroelectric. $T_{CW}$ is obtained by fitting the reciprocal of the dielectric constant of the sample at 1 MHz. The relationship between the reciprocal of dielectric constant ($1/\varepsilon$) and temperature is shown in Fig. 8(a). It can be found that the ceramic materials studied do not fully conform to the Curie-Weiss law, but can only be fully satisfied at higher than a certain temperature. When $T > T_m$, the values of $\ln(1/\varepsilon - 1/\varepsilon_m)$ and $\ln(T - T_m)$ at 1 MHz frequency are expressed in coordinates, where $\ln(1/\varepsilon - 1/\varepsilon_m)$ is the ordinate and $\ln(T - T_m)$ the abscissa. The calculation results are shown in Fig. 8(b). After calculation and fitting, $\gamma = 1.394 \pm 0.00741$ is obtained, and it is found that the ceramic is a typical relaxation ferroelectric.

Fig. 9(a) shows the $P$-$E$ hysteresis loops of (1 –$x$)KNN-$x$BZN ceramic samples measured at room temperature and frequency is 1 Hz. As observed, with increasing BZN content, the hysteresis loop turns from saturated to unsaturated, and finally has a tendency to saturated. When $x$ = 0.07 and 0.08, the hysteresis loop is slender compared with that of other components, which indicates that the electric domain deflection of the component ceramics responds more rapidly to the applied electric field, and the hysteresis decreases, which is consistent with the conclusion of the dielectric temperature spectrum. It can be found from Fig. 9(b) that the residual polarization strength ($P_r$) and coercive field ($E_c$) of the specimens decrease to their lowest values at $x$ = 0.08, that is 1.477 μC/cm$^2$ and 8.28 kV/cm, respectively. Because of the high symmetry of the pseudo-cubic phase, the electric domain deflects under the stimulation of a smaller external electric field, which reduces $P_r$ and $E_c$, that is resistance of the ceramics to an external electric field.

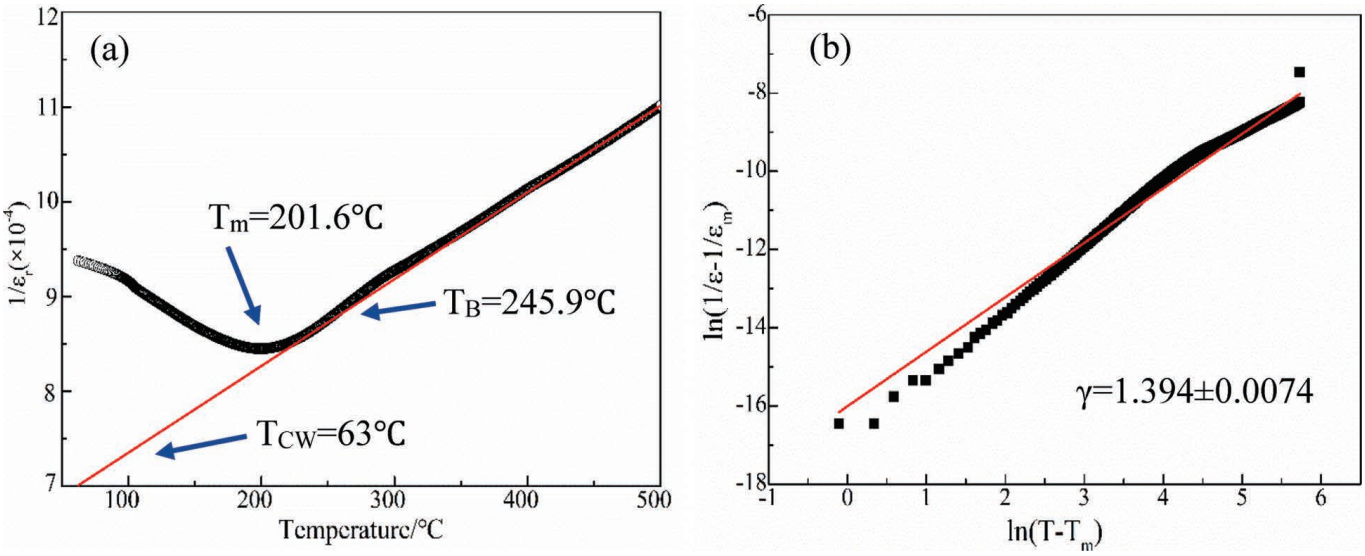


**Fig. 8:** (a) Reciprocal diagram of dielectric constant of 0.97KNN-0.07BZN at 1 MHz. (b) Linear relationship between $\ln(1/\varepsilon\text{-}1/\varepsilon_m)$ and $\ln(T\text{-}T_m)$.

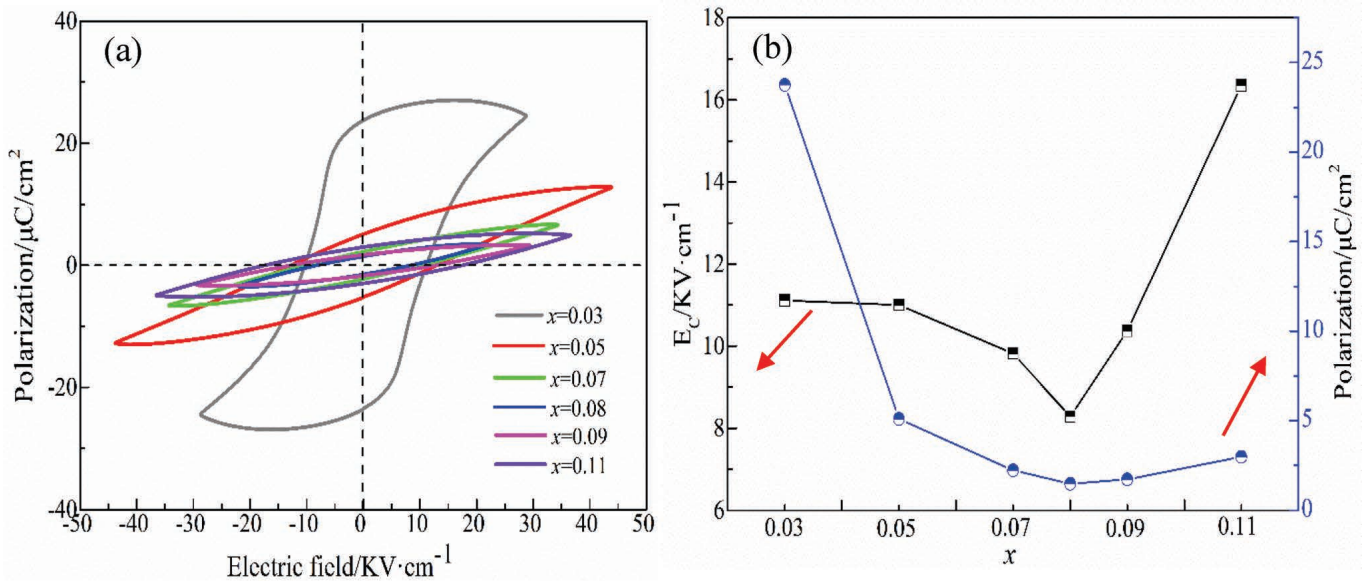


**Fig. 9:** (a) *P-E* loops of (1-*x*)KNN-*x*BZN ceramics. (b) Change of $P_r$ and $E_c$ with variation of *x*.

## IV. Conclusions

In this work, (1 –*x*)KNN-*x*BZN transparent electro-optic ceramics were prepared by means of the solid-state reaction technique, and the effects of BZN content on their microstructure, phase transition, optical properties, and electrical properties were systematically investigated. With increasing BZN content, the crystal structure transforms from the orthorhombic phase into the pseudo-cubic phase and finally to the tetragonal phase. Ceramics with high relative density, low apparent porosity, and uniform and fine-grained microstructures were obtained with addition of $Ba(Zn_{1/3}Nb_{2/3})O_3$. The KNN-BZN ceramics with $x = 0.07$ displayed the highest transmittance, that is 43.00 % at 780 nm in the visible spectrum, and $\varepsilon_r$, tanδ, $P_r$ and $E_c$ were 975.9, 0.02, 2.231 μC/cm² and 9.82 kV/cm, respectively, and after comprehensive comparison, the performance exhibited at these values proved the best. The study of the KNN-BZN transparent piezoelectric ceramic can be helpful in the design and synthesis of other KNN-based ceramics with high transmittance.

## References


1 Masahiro, N., Yamaguchi, K., Toki, M.: $ZrO_2$-$Al_2O_3$ composite ceramic material and production method thereof. US Patent 7012036 (2006). http://www.freepatentsonline.com/7012036.html

2 Wang, S.F., Zhang, J., Luo, D.W., Gu, F., Tang, D.Y., Dong, Z.L., Tan, G.E.B., Que, W.X., Zhang, T.S., Li, S., Kong, L.B.: Transparent ceramics: processing, materials and applications, *Prog. Solid State Ch.*, **41**, 20–54, (2013) https://doi.org/10.1016/j.progsolidstchem.2012.12.002

3 Haertling, G.H.: Improved hot-pressed electrooptic ceramics in the $(Pb,La)(Zr,Ti)O_3$ system, *J. Am. Ceram. Soc.*, **54**, [6], 303–309, (1971). https://doi.org/10.1111/j.1151–2916.1971.tb12296.x

4 Haertling, G.H.: PLZT electrooptical materials and applications – a review, *Ferroelectrics*, **75**, 25–55, (1987). https://doi.org/10.1080/00150198708008208

5 Li, K.K., Wang, W.Q.: Electro-optic ceramic material and device, WIPO Patent Application WO/2003/099740 (2003). http://www.freepatentsonline.com/$WO_2$003099740.html

6 Jiang, H., Zou, Y.K., Chen, Q., Li, K.K., Zhang, R., Wang, Y.: Transparent electro-optic ceramics and devices, *Optoelectronic Devices and Integration*, **5644**, 380 – 394, (2005).

7 Du, H.L., Tang, F.S., Liu, D.J., Zhu, D.M., Zhou, W.C., Qu, S.B.: The microstructure and ferroelectric properties of $(K_{0.5}Na_{0.5})NbO_3$ –$LiNbO_3$ lead-free piezoelectric ceramics, *B Mater. Sci. Eng.*, **136**, 165 – 169, (2007). https://doi.org/10.1016/j.mseb.2006.09.031

8 Du, H.L., Liu, D.J., Tang, F.S., Zhu, D.M., Zhou, W.C.: Microstructure, piezoelectric, and ferroelectric properties of $Bi_2O_3$-added $(K_{0.5}Na_{0.5})NbO_3$ lead-free ceramics, *J. Am. Ceram. Soc.*, **90**, [9] 2824 – 2829, (2007). https://doi.org/10.1111/j.1551 – 2916.2007.01846.x

9 Du, H.L., Zhou, W.C., Zhu, D.M., Fa, L., Qu, S.B., Li, Y., Pei, Z.B.: Sintering characteristic, microstructure, and dielectric relaxor behavior of $(K_{0.5}Na_{0.5})NbO_3$-$(Bi_{0.5}Na_{0.5})TiO_3$ lead-free ceramics, *J. Am. Ceram. Soc.*, **91**, [9], 2903 – 2909, (2008). https://doi.org/10.1111/j.1551 – 2916.2008.02528.x

10 Li, K., Li, F.L., Wang, Y., Kwok, K.W., Chan, H.L.W.: Hot-pressed $K_{0.48}Na_{0.52}Nb_{1-x}Bi_xO_3$ (x = 0.05 – 0.15) lead-free ceramics for electro-optic applications, *Mater. Chem. Phys.*, **131**, 320 – 324, (2011). https://doi.org/10.1016/j.matchemphys.2011.09.048

11 Li, F.L., Kwok, K.W.: Fabrication of transparent electro-optic $(K_{0.5}Na_{0.5})_{1-x}Li_xNb_{1-x}Bi_xO_3$ lead-free ceramics, *J. Eur. Ceram. Soc.*, **33**, 123 – 130, (2013). https://doi.org/10.1016/j.jeurceramsoc.2012.08.017

12 Liu, Z.Y., Fan, H.Q., Zhao, Y.W., Dong, G.Z.: Optical and tunable dielectric properties of $K_{0.5}Na_{0.5}NbO_3$-$SrTiO_3$ ceramics, *J. Am. Ceram. Soc.*, **99**, [1], 146 – 151, (2016). https://doi.org/10.1111/jace.13864

13 Liu, Z.Y., Fan, H.Q., Lei, S.H., Wang, J., Tian, H.L.: Fatigue properties and impedance analysis of potassium sodium niobate-strontium titanate transparent ceramics, *Appl. Phys. A-Mater.*, **122**, [10], 900, (2016). https://doi.org/10.1007/s00339 – 016 – 0437 – 5

14 Liu, Z.Y., Fan, H.Q., Peng, B.L.: Enhancement of optical transparency in $Bi_2O_3$-modified $(K_{0.5}Na_{0.5})_{(0.9)}Sr_{0.1}Nb_{0.9}Ti_{0.1}O_3$ ceramics for electro-optic applications, *J. Mater. Sci.*, **50**, [24], 7958 – 7966, (2015). https://doi.org/10.1007/s10853 – 015 – 9360-y

15 ] Liu, Z.Y., Fan, H.Q., Lei, S.H., Ren, X.H., Long, C.B.: Duplex structure in $K_{0.5}Na_{0.5}NbO_3$-$SrZrO_3$ ceramics with temperature-stable dielectric properties, *J. Eur. Ceram. Soc.*, **37**, [1], 115 – 122, (2017). https://doi.org/10.1016/j.jeurceramsoc.2016.07.024

16 Long, C.B., Li, T.Y., Fan, H.Q., Wu, Y., Zhou, L.C., Li, Y.W., Xiao, L.H., Li, Y.H.: Li-substituted $K_{0.5}Na_{0.5}NbO_3$-based piezoelectric ceramics: crystal structures and the effect of atmosphere on electrical properties, *J. Alloy. Compd.*, **658**, 839 – 847, (2016). https://doi.org/10.1016/j.jallcom.2015.10.245

17 Sui, J.N., Fan, H.Q., Hu, B., Ning, L.: High temperature stable dielectric properties and enhanced energy-storage performance of $(1\text{-}x)(0.85Na_{0.5}Bi_{0.5}TiO_3\text{-}0.15Ba_{0.8}Ca_{0.2}Ti_{0.8}Zr_{0.2}O_3)\text{-}xK_{0.5}Na_{0.5}NbO_3$ lead-free ceramics, *Ceram. Int.*, **44**, [15], 18054 – 18059, (2018). https://doi.org/10.1016/j.ceramint.2018.07.008

18 Wang, Y.Y., Yang, H., Zhang, Q.L.: Phase structure and polar characteristics of alkali niobate ceramics modified by $Ba_{0.6}Ca_{0.4}ZrO_3$, *Ceram. Int.*, **42**, 929 – 935, (2016). http://dx.doi.org/10.1016/j.ceramint.2015.09.021

19 Yang, D., Ma, C., Yang, Z.P., Wei, L.L., Chao, X.L., Yang, Z.Y., Yang, J.L.: Optical and electrical properties of pressureless sintered transparent $(K_{0.37}Na_{0.63})NbO_3$-based ceramics, *Ceram. Int.*, **42**, 4648 – 4657, (2016). https://doi.org/10.1016/j.ceramint.2015.11.032

20 Chai, Q.Z., Zhao, X.M., Chao, X.L., Yang, Z.P.: Enhanced transmittance and piezoelectricity of transparent $K_{0.5}Na_{0.5}NbO_3$ ceramics with $Ca(Zn_{1/3}Nb_{2/3})O_3$ additives, *RSC Adv.*, **7**, 28428, (2017).

21 Lin, C., Wu, X., Lin, M., Huang Y.P., Li, J.: Optical, luminescent and optical temperature sensing properties of $(K_{0.5}Na_{0.5})NbO_3$-$ErBiO_3$ transparent ceramics, *J. Alloy. Compd.*, **706** 156 – 163, (2017). http://dx.doi.org/10.1016/j.jallcom.2017.02.245